



# Hydrothermal Synthesis of Single-Domain Zinc Ferrite Nanoparticles ( $\text{ZnFe}_2\text{O}_4$ ): Structural, Morphological, and Magnetic Studies

Gassem M. Alzoubi<sup>1</sup>

Received: 9 January 2022 / Accepted: 13 March 2022 / Published online: 18 April 2022  
© The Author(s), under exclusive licence to Springer Science+Business Media, LLC, part of Springer Nature 2022

## Abstract

In order to investigate the size dependence of magnetic properties in the single-domain and superparamagnetic regimes, zinc ferrite  $\text{ZnFe}_2\text{O}_4$  nanoparticles were synthesized with sizes around 15 nm by the hydrothermal method. The zinc ferrite nanoparticles were characterized by XRD, TEM, FT-IR, and VSM. According to the Rietveld refinement results, the nanoparticles exhibited a cubic single-phase spinel-type structure. The TEM observations indicated that the nanoparticles were spherical in shape. The FT-IR analysis revealed two dominant absorption bands, confirming the formation of a single-phase spinel structure with two sub-lattices: tetrahedral and octahedral. Magnetic measurements conducted over a wide range of temperatures and magnetic fields revealed that the ferrite nanoparticles were ferrimagnetic dressed with spin-glass behavior below the blocking temperature ( $T_B$ ) and superparamagnetic above  $T_B$ . The saturation magnetization and the first anisotropy constant of the nanoparticles were found to increase with decreasing temperature. The superparamagnetic critical size,  $D_{SP}$ , of the nanoparticles was found to be about 13 nm, suggesting that the prepared ferrite nanoparticles were within the superparamagnetic regime, and thus by implication within the single domain regime.

**Keywords** Zinc ferrite · Single-domain · Rietveld refinement · Spin glass · TEM · ZFC-FC curves

## 1 Introduction

Magnetic ferrite nanoparticles have attracted considerable interest due to their high potential for use in a variety of technological domains, including ferrites-based permanent magnets, gas sensors, magnetic and electronic devices, and pharmaceutical applications [1–6]. Zinc ferrite ( $\text{ZnFe}_2\text{O}_4$ ) is particularly interesting because it has been used in a variety of applications including hyperthermia treatment of cancer [7], gas sensor [8], and semiconductor photo catalysts [9].

Zinc ferrite possesses a cubic normal-spinel structure with a space group of  $Fd\bar{3}m$ . The oxygen ions in this structure form a cubic close-packed FCC lattice, with  $\text{Zn}^{2+}$  ions occupy the tetrahedral (A sites) and  $\text{Fe}^{3+}$  ions occupy octahedral (B sites) that can be represented by the formula  $(\text{Zn}^{2+})_A[\text{Fe}^{3+}]_B\text{O}_4$  [10]. Zinc ferrite nanoparticles have been synthesized using a variety of methods, including

co-precipitation [1], hydrothermal [11], sol-gel [12], solid state reactions [13] and high energy ball milling [14].

In order to be used in a wide variety of applications, the size and shape of these nanoparticles should be optimized in a controlled manner. This is attributable to the fact that the magnetic properties of magnetic nanoparticles vary dramatically with size. However, most previous studies on zinc ferrites were carried out in the multi-domain regime, where the usual size of produced nanoparticles was substantially larger than the single-domain critical size, resulting in very little size dependence of their magnetic properties [15, 16]. This is due to the difficulty of synthesizing ultra-small and monodisperse nanoparticles in this field. The primary goal of this work is to synthesize monodisperse and single-phase  $\text{ZnFe}_2\text{O}_4$  ferrite nanoparticles with typical sizes in the single-domain regime, as well as to analyze their structural and magnetic characteristics in detail. Understanding the magnetic properties of these stable ferrite nanoparticles, as well as having a repeatable recipe for producing them in a single-domain regime, is a necessary first step toward their being used in a variety of applications, mainly in cancer treatment and gas sensors [7, 8].

✉ Gassem M. Alzoubi  
Gassem@hu.edu.jo

<sup>1</sup> Department of Physics, Faculty of Science, The Hashemite University, 330127, Zarqa 13133, Jordan

## 2 Materials and Methods

### 2.1 Starting Materials

The starting materials used in this work were: zinc nitrate hexahydrate  $\text{Zn}(\text{NO}_3)_2 \cdot 6\text{H}_2\text{O}$  of 98% purity, iron (III) nitrate nonhydrate  $\text{Fe}(\text{NO}_3)_3 \cdot 9\text{H}_2\text{O}$  of 98% purity, sodium hydroxide  $\text{NaOH}$  of 98% purity, HPLC plus deionized water (DI), and ethanol absolute anhydrous (ACS reagent). All chemicals in this study were used as-received.

### 2.2 Synthesis Procedure

In this work, the hydrothermal method was used to make the  $\text{ZnFe}_2\text{O}_4$  ferrite nanoparticles [16, 17]. In a conventional hydrothermal synthesis process, 10 mmol of Fe(III) nitrate and 5 mmol of Zn(II) nitrates were mixed in 140 mL of deionized water under magnetic stirring for 10 minutes at 500 rpm. After thoroughly mixing, an aqueous solution of 60 mmol  $\text{NaOH}$  dissolved in 20 mL DI water was added dropwise to the aforementioned solution while being vigorously stirred ( $\sim 1400$  rpm). The concentration of nitrates in the total solution was maintained below 0.12 mol/L to produce essentially monodisperse nanocrystals [16]. The final solution was left under stirring for 15 minutes at a high speed of  $\sim 1400$  rpm. After that, the solution was poured into a Teflon reactor and placed in an autoclave system, which was then placed in an oven for thermal treatment. The autoclave was kept at  $190^\circ\text{C}$  in the oven for 12 hours before being removed from the oven and allowed to cool naturally to 300 K. The resulting powder was separated from the solution by centrifugation at 4500 rpm and washed several times with ethanol and DI water. The resulting powder was then dried for a day at  $105^\circ\text{C}$  in a drying oven before being crushed with a mortar and pestle, yielding approximately  $\sim 1$  g of finished product. Finally, the nanoparticles were annealed for 6 hours at  $700^\circ\text{C}$  in a tube furnace. High-temperature annealing is important because it improves the crystallinity of the ferrite nanoparticles. However, annealing the nanoparticles at temperatures above  $700^\circ\text{C}$  is not recommended because it may induce particle growth beyond the prepared ferrite nanoparticles single-domain size limit [16].

### 2.3 Characterization Techniques

Various techniques were used to characterize the prepared nanoparticles. The X-ray diffraction (XRD) measurements were taken on Rigaku Ultima IV diffractometer with  $\text{Cu} - \text{K}_\alpha$  radiation source ( $\lambda = 0.15406$  nm). The measurements range was set from  $2\theta = 16 - 70^\circ$ , with a scanning speed of  $2^\circ/\text{min}$ . The surface morphology, average size, and

size distribution of the nanoparticles were examined using JEOL 1200 transmission electron microscope (TEM). The Fourier transform infrared (FT-IR) spectrum of the resulting powder was measured using a Bruker Vertex 70 FTIR spectrometer. Magnetic measurements were taken using a Quantum Design PPMS equipped with a vibrating sample magnetometer (VSM) at temperatures ranging from 10 to 300 K and in a vertical magnetic field of up to 25 kOe.

## 3 Results and Discussion

### 3.1 X-ray Diffraction and Structural Analysis

Figure 1 shows X-ray diffraction (XRD) pattern of the  $\text{ZnFe}_2\text{O}_4$  ferrite nanoparticles. As shown in the figure, all peaks were assigned to the cubic space group  $\text{Fd}\bar{3}\text{m}$ , confirming the single-phase formation of the prepared ferrite nanoparticles with no impurity phases. All visible peaks are consistent with standard powder XRD data of zinc ferrite (PDF # 73-1963), which are depicted at the bottom of the figure as vertical black bars [16]. The sample's high peak intensity implies that annealing at a high temperature improved crystallinity.

The Rietveld refinement of the ferrite nanoparticles was carried out using the FullProf software [18]. Table 1 and Fig. 1 show the outcome of this refinement. The goodness of fit (GoF) was used to evaluate the Rietveld fitting quality after each refinement cycle, where  $(\text{GoF} = (\text{R}_{\text{wp}}/\text{R}_{\text{exp}})^2)$ , with  $\text{R}_{\text{wp}}$  and  $\text{R}_{\text{exp}}$  are the weighted profile and expected values of the agreement R-factors, respectively. Taking into account the normal spinel structure of zinc ferrite, all

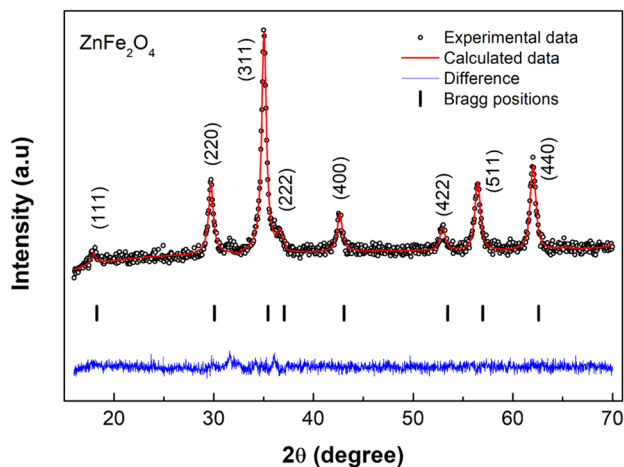


**Fig. 1** (color online) XRD powder pattern and Rietveld refinement of the  $\text{ZnFe}_2\text{O}_4$  ferrite nanoparticles. The experimental data are represented by black circles, the calculated data by a red line, and the difference between the two by a blue line. Bragg positions are represented by black vertical bars

**Table 1** Structural parameters and Rietveld agreement R-factors for ZnFe<sub>2</sub>O<sub>4</sub> ferrite nanoparticles. The description of the parameters is given in the text

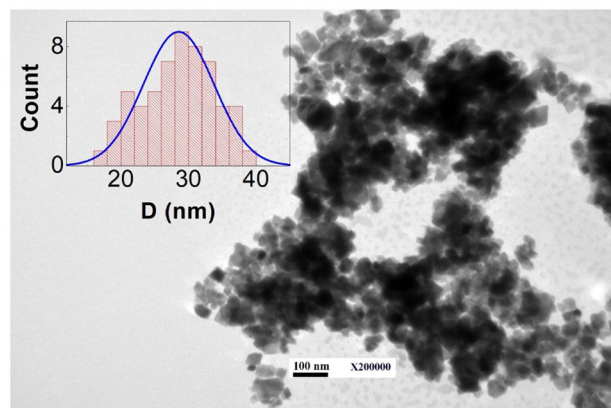
Quantity	Refined value
D(nm)	15.0
$d_x$ (g/cm <sup>3</sup> )	5.35
<i>Residual factors (%)</i>	
$R_{exp}$	1.537
$R_{wp}$	1.720
GoF ( $\chi^2$ )	1.25
<i>Cell parameters (Å)</i>	
$a_{exp}$	8.4263
$u$	0.2731
$R_A$	2.1615
$R_B$	1.9316

cations were distributed between tetrahedral (8a) and octahedral (16d) positions while maintaining the ZnFe<sub>2</sub>O<sub>4</sub> ferrites' stoichiometric composition [17, 19]. Assuming that oxygen anions form a perfect cubic closed packing (CCP) lattice and that the unit cell's origin is located in an octahedral vacancy [17], the ideal value of  $u$  is 0.25 Å [19]. However, in real spinel ferrites, oxygen anions are somewhat drifted away from their perfect CCP locations, significantly affecting bond lengths and angles. As shown in Table 1, the measured value of  $u$  is 0.2731 Å which is consistent with reported value of 0.2582 Å for ZnFe<sub>2</sub>O<sub>4</sub> [20]. The estimated experimental lattice constant ( $a_{exp}$ ) is 8.4263 Å which is consistent with reported results of 8.4363 Å [20], 8.4322 Å [12], and 8.430 Å [21].

The average bond lengths at the tetrahedral ( $R_A$ ) and octahedral ( $R_B$ ) sites can be calculated using the relations given in my previous publication [16]. Table 1 displays the refined  $R_A$  and  $R_B$  values. The  $R_A$  value is found to be higher than the  $R_B$  value. This is expected as the tetrahedral (A sites) are occupied by the Zn<sup>2+</sup> ions with radius of 0.81 Å, whereas the octahedral (B sites) are occupied by the Fe<sup>3+</sup> ions with smaller radius of 0.66 Å. The measured X-ray density,  $d_x = 5.35$  g/cm<sup>3</sup>, matches the reported value of 5.35 g/cm<sup>3</sup> of the ZnFe<sub>2</sub>O<sub>4</sub> ferrite nanoparticles prepared via sol-gel route and annealed at 1000 C° [12]. The average crystallite size,  $D$ , of the ferrite sample was evaluated by measuring the full width at half maxima (FWHM) of the most intense peak (311) from XRD pattern and by using the Scherrer equation [16]. As shown in Table 1, the obtained value of  $D$  is 15 nm.

### 3.2 TEM Analysis

Figure 2 displays a TEM image of ZnFe<sub>2</sub>O<sub>4</sub> ferrite nanoparticles as well as the particle size distribution. The

**Fig. 2** (color online) TEM image and particle size distribution of the ZnFe<sub>2</sub>O<sub>4</sub> ferrite nanoparticles taken at high magnification of 200,000

nanoparticles have an approximately spherical shape, as illustrated in the figure, suggesting that the recipe generated monodisperse spherical nanoparticles successfully. The estimated average particle size obtained from TEM observations (~ 28 nm), as shown in the inset of Fig. 2, is almost double that obtained from XRD measurements (15.0 nm). A similar trend was observed for Zn<sub>x</sub>Co<sub>1-x</sub>Fe<sub>2</sub>O<sub>4</sub> ferrite nanoparticles synthesized via the coprecipitation method, where the average particle size was found to be nearly three times larger than the average crystallite size [21]. Because XRD measures average crystallite size, whereas TEM measures average particle size, which might be made up of many crystallites, the difference is to be expected [16].

### 3.3 FT-IR Analysis

Figure 3 displays the measured FT-IR spectrum of the ZnFe<sub>2</sub>O<sub>4</sub> ferrite nanoparticles in the wave number range of 370–800 cm<sup>-1</sup>. For ferrites with spinel type structure, it is expected to have four modes of vibrations occurring in the  $\nu_1$  (650 – 550 cm<sup>-1</sup>),  $\nu_2$  (525 – 390 cm<sup>-1</sup>),  $\nu_3$  (380 – 335 cm<sup>-1</sup>) and  $\nu_4$  (300 – 200 cm<sup>-1</sup>) regions [22]. As shown in the figure, there are two main metal-oxygen bands at frequencies ~ 532 and 396 cm<sup>-1</sup>. The stretching vibrations of the Zn-O bond in the tetrahedral sites produce the higher frequency band. The Fe-O bond vibrations at the octahedral sites produce the lower frequency one. The creation of a single-phase spinel structure with two sub-lattices (tetrahedral and octahedral) is confirmed by these absorption bands [23]. As shown in the figure, there is a shoulder peak in the tetrahedral region occurring at ~ 620 cm<sup>-1</sup>, suggesting that the tetrahedral site is often occupied by more than one cation. It can therefore be deduced that the synthesized ferrite nanoparticles are most likely mixed spinel-type structure. Similar shoulder peak occurring in the tetrahedral region was observed in the same ZnFe<sub>2</sub>O<sub>4</sub> ferrite system

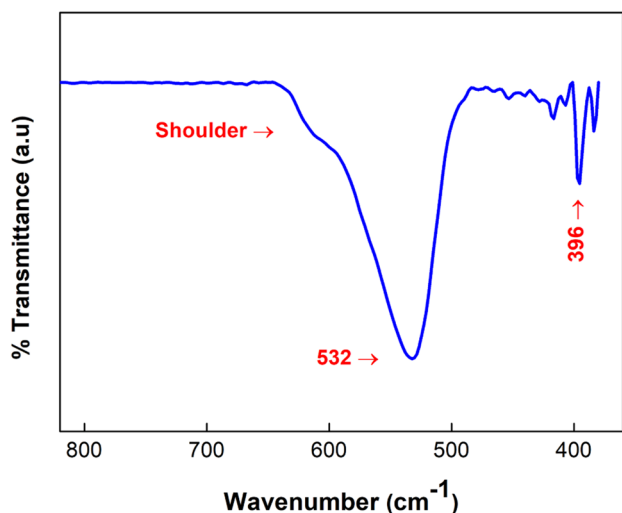


**Fig. 3** (color online) Room temperature FT-IR absorption spectrum for the  $\text{ZnFe}_2\text{O}_4$  ferrite nanoparticles in the wave number range of  $370 - 800 \text{ cm}^{-1}$

prepared by the sol–gel autocombustion method [24]. The  $\nu_3$  and  $\nu_4$  absorption bands could not be observed as they are located in the far-infrared region, which is beyond the measuring range of the FT-IR machine used in recording the FT-IR spectra.

### 3.4 Magnetic Properties

#### 3.4.1 M vs H Curves

Figure 4(a) shows magnetic hysteresis loops for  $\text{ZnFe}_2\text{O}_4$  ferrite nanoparticles obtained at various temperatures with a magnetic field spanning from  $-25 \text{ kOe}$  to  $25 \text{ kOe}$ . As shown in the figure, and based on the shape of the hysteresis loops, the presence of either ferrimagnetic or superparamagnetic phases can be seen depending on the temperature. Above  $100 \text{ K}$ , the ferrite nanoparticles exhibit no hysteresis, indicating that they are superparamagnetic over this temperature range. This is demonstrated by the sigmoidal shape of their corresponding M-H curves with nearly zero coercivity and zero remanence. The appearance of this superparamagnetic behavior is attributed to the small size nature of the prepared ferrite nanoparticles being in the single domain regime. However, at  $10 \text{ K}$ , the ferrite nanoparticles show ferrimagnetic behavior with well-defined saturation magnetization ( $M_s \sim 20 \text{ emu/g}$ ), coercivity ( $H_C \sim 420 \text{ Oe}$ ), and remanence ( $M_r \sim 6 \text{ emu/g}$ ) as shown in Fig. 4(b). The unexpected presence of ferrimagnetism at  $10 \text{ K}$  can be explained as follows. It is well known that bulk  $\text{ZnFe}_2\text{O}_4$  ferrite is antiferromagnetic material below its Neel's temperature ( $T_N \approx 9 - 11 \text{ K}$ ) and is paramagnetic above it [15]. This is because bulk

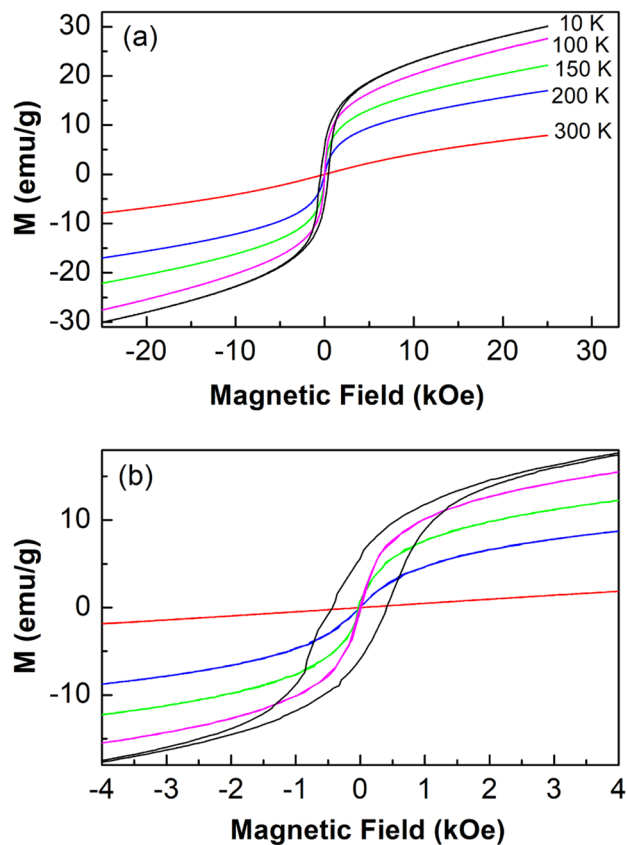


**Fig. 4** (color online) (a) Magnetization curves of the  $\text{ZnFe}_2\text{O}_4$  ferrite nanoparticles taken at various temperatures and shown over an extended magnetic field from  $-25 \text{ kOe}$  to  $25 \text{ kOe}$ . (b) A magnified view of all the M-H curves over an applied field from  $-4 \text{ kOe}$  to  $4 \text{ kOe}$  showing the low magnetic field behavior

zinc ferrite crystallizes into an ideal normal spinel structure in which the tetrahedral (A sites) are occupied by the  $\text{Zn}^{2+}$  ions and the octahedral (B sites) are occupied by the  $\text{Fe}^{3+}$  ions. Knowing that the  $\text{Zn}^{2+}$  ion has zero magnetic moment and that the  $\text{Fe}^{3+}$  ions are antiparallel to each other on the B sites, the bulk zinc ferrite has zero net magnetic moment. On the other hand, it is also known that in spinel ferrites, particle size and distribution of cations between the tetrahedral and octahedral sites play an important role in determining magnetic properties of these ferrites. Generally speaking, the magnetization is enhanced with reducing the size of these ferrite nanoparticles. This increasing tendency of the magnetization with reducing particle size can be attributed to a variation in the site distribution in these nanoparticles [25]. We therefore deduce that the ferrimagnetic behavior observed in zinc ferrite nanoparticles at  $10 \text{ K}$  can be understood by assuming that these ferrite nanoparticles have a mixed spinel structure, which is responsible of producing imbalanced magnetic moments between the tetrahedral and octahedral sites.



### 3.4.2 LA Approach

Figure 4 shows that with the maximum applied magnetic field of 25 kOe, saturation magnetization is not achieved. Therefore, the law of approach to saturation (LA) was used to calculate the saturation magnetization ( $M_s$ ) and the first anisotropy constant ( $K_1$ ). This approach is typically good for describing magnetization near saturation and is valid at fields much higher than the coercive field ( $H \gg H_c$ ) [26]. The magnetization ( $M$ ) near the saturation is determined by [26]

$$M = M_s \left(1 - \frac{b}{H^2}\right) + \kappa H \tag{1}$$

where  $b = \frac{8}{105} \frac{K_1^2}{\mu_0^2 M_s^2}$ ,  $M_s$  is the saturation magnetization,  $H$  is the applied field,  $\mu_0$  is free-space magnetic permeability, and  $K_1$  is the first anisotropy constant (also known as the cubic anisotropy constant). The last term,  $\kappa H$ , often referred to as a paramagnetism-like term [27]. This term was found to be required in order to fit the obtained data. Figure 5 shows the magnetization curves for  $ZnFe_2O_4$  ferrite nanoparticles fitted to the LA model at various temperatures. Because the LA

model accurately describes magnetization at high fields, our fit was limited to magnetization data taken from 10 to 25 kOe. Table 2 summarizes the  $M_s$  and  $K_1$  values derived from the fit, as well as the  $H_c$  and  $M_r$  values. The variation of  $M_s$  and  $K_1$  with temperature is shown in the bottom right corner of Fig. 5. The  $M_s$  value obtained at room temperature (3 emu/g) was found to be greater than the  $M_s$  value of the bulk zinc ferrite (0 emu/g). Again, this can be due to the imbalance in the magnetic moments at the A and B sites created by the mixed-spinel structure proposed early for zinc ferrite. At 10 K, the obtained  $M_s$  value of 20 emu/g is consistent with the reported value of 38 emu/g for zinc ferrite nanoparticles having size of 13.4 nm and measured at 5 K [25]. As demonstrated in the bottom right corner of Fig. 5, the variation of  $M_s$  with temperature increased with decreasing temperature. The  $K_1$  value obtained at RT ( $0.3 \times 10^6$  erg/cm<sup>3</sup>) is close to the RT reported value of  $0.2 \times 10^6$  erg/cm<sup>3</sup> [28]. The obtained  $K_1$  values were similarly found to increase as the temperature was reduced. This is to be expected, since decreasing temperature increases magnetic anisotropy. It is well established that superparamagnetic particles are paramagnetic above the blocking temperature, and thus  $M(H)$  should be linear. Figure 5 shows, on the other hand, that the high-field magnetization is not linear at 300 K. This nonlinear behavior could be attributed to a small amount of an external Fe-based phase that was not detected in XRD.

### 3.4.3 M vs T Curves

The ZFC-FC Magnetization curves were obtained by the well-known procedure described in reference [17]. Figure 6 displays the ZFC-FC magnetization curves of the  $ZnFe_2O_4$  ferrite nanoparticles measured at various applied magnetic fields ranging from 25 Oe to 1000 Oe. As shown in the figure, the ZFC curves show a broad peak at specific temperature that is dependent on the applied field. This peak is caused by both superparamagnetic behavior (with blocking temperature  $T_B$ ) and spin-glass like behavior (with freezing temperature  $T_g$ ). Because they are overlapping, it is

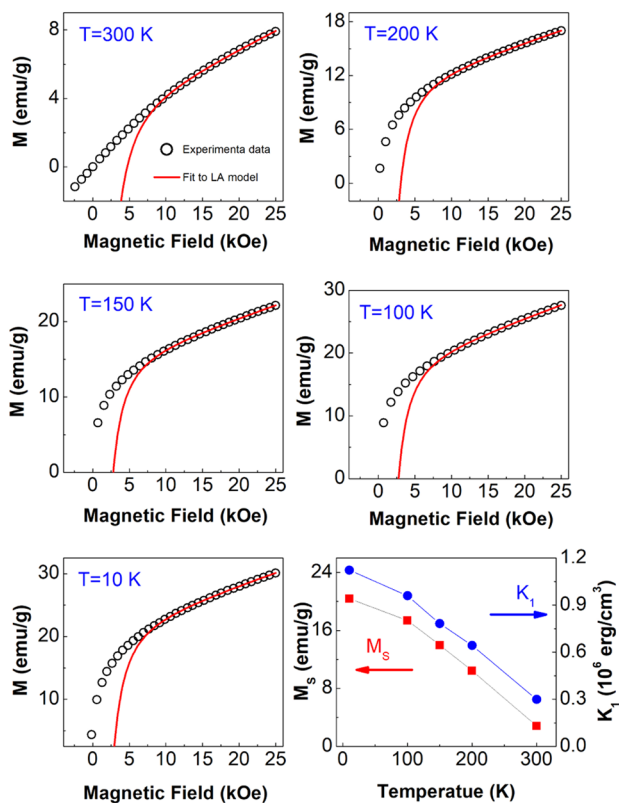


**Fig. 5** (color online) Magnetization curves of the  $ZnFe_2O_4$  ferrite nanoparticles measured at various temperatures and fitted to the LA model. The figure in the bottom right corner depicts the variation of saturation magnetization ( $M_s$ ) and first anisotropy constant ( $K_1$ ) with temperature

**Table 2** Magnetic parameters for the  $ZnFe_2O_4$  ferrite nanoparticles measured at different temperatures. The description of the parameters is given in the text

Temperature (K)	$M_r$ (emu/g)	$H_c$ (Oe)	$M_s$ (emu/g)	$K_1$ (erg/cm <sup>3</sup> )
300	0	0	2.8	$0.30 \times 10^6$
200	0	0	10.5	$0.65 \times 10^6$
150	0	0	14.0	$0.78 \times 10^6$
100	0	0	17.4	$0.96 \times 10^6$
10	5.7	420	20.4	$1.12 \times 10^6$

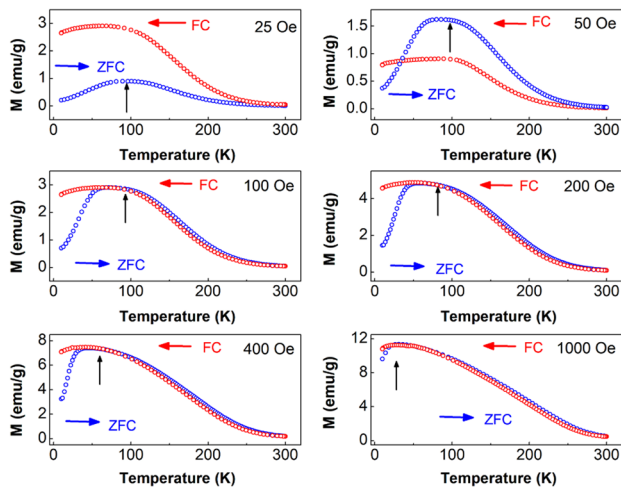


**Fig. 6** (color online) ZFC-FC Magnetization curves of the  $\text{ZnFe}_2\text{O}_4$  ferrite nanoparticles measured at various magnetic fields

impossible to distinguish  $T_B$  from  $T_g$  in this case. However, the superparamagnetic behavior is evident by the Curies law-like behavior above  $T_B$ . By raising the temperature above  $T_B$ , the thermal energy exceeds the magnetic anisotropy energy, and the nanoparticles gain enough thermal energy to randomize their moments, reducing the overall magnetization of these ferrites with increasing temperature and becoming superparamagnetic. This is consistent with the corresponding M-H curves measured above 100 K that have almost zero coercivity and zero remanence. For  $T < T_B$ , the nanoparticles show weak ferrimagnetic behavior with small coercivity as evidenced from the corresponding M-H curve at 10 K (see Fig. 4). Consequently, the zinc ferrite nanoparticles have a superparamagnetic behavior for  $T > T_B$  and ferrimagnetic behavior for  $T < T_B$ . Furthermore and as shown in the ZFC curves, the blocking temperature,  $T_B$ , is field dependent. By further increasing the applied magnetic field,  $T_B$  shifts down to lower temperatures. The estimated value of ( $T_B \approx 95$  K) measured with an applied field of 25 Oe is almost twice that reported in [29] and four times bigger than that reported in [30]. This discrepancy in measured  $T_B$  values for zinc ferrite is due to the fact that the blocking temperature is sensitive to several factors such as synthesis method, annealing temperature, and size distribution. The slowly changing magnetization of the FC curves for  $T < T_B$ , on the other hand, is a sign of spin-glass like behavior caused by non-negligible dipole–dipole interactions between the ferrimagnetic nanoparticles [31]. The nanoparticles appear to be ferrimagnetic dressed with spin-glass behavior below  $T_B$  and superparamagnetic above  $T_B$ . To further confirm the superparamagnetic nature of these nanoparticles above  $T_B$ , we calculated the critical size ( $D_{SP}$ ) for a spherical nanoparticle to enter the superparamagnetic regime from above using [16]

$$D_{SP} = 2 \left( \frac{6 k_B T_B}{K} \right)^{1/3} \quad (2)$$

where  $K$  is the magnetic anisotropy energy. For the zinc ferrite nanoparticles at RT and using  $T_B \approx 95$  K (estimated with an applied field of 25 Oe) and  $K = K_1 = 0.3 \times 10^6$  erg/cm<sup>3</sup>, the obtained value of  $D_{SP}$  is  $\sim 13$  nm. This value of  $D_{SP}$  is similar to the value of the crystallite size (15 nm) obtained from XRD analysis (see Table 1), indicating that the prepared ferrite nanoparticles are indeed superparamagnetic above  $T_B$ . Since superparamagnetism of nanoparticles assumes the existence of a single domain [32], we conclude that the prepared zinc ferrite nanoparticles lay within the single domain regime. Finally, it is worth noting that the M vs T data taken at 50 Oe is unusual in that the FC curve is below the ZFC. This is usually not the case because the FC curve should be higher than the ZFC curve. This could be because the sample was not completely demagnetized at RT, leaving some remanent magnetization. During field cooling, this remanent magnetization is quenched rather than a homogeneously random one, lowering the FC curve slightly below the ZFC curve.

Finally, it is worth noting that the M vs T data taken at 50 Oe is unusual in that the FC curve is below the ZFC. This is usually not the case because the FC curve should be higher than the ZFC curve. This could be due to competition between various magnetic interactions in nanoparticles under low fields, such as FM, AFM, and canted spin structures [33]. On average, these interactions may result in a frustrated spin system that generates anomalous behavior of temperature dependent magnetization curves, with higher ZFC values than FC under 100 Oe [33]. When compared to curves measured at 25 Oe and 100 Oe, this anomalous behavior reduces the ZFC and FC curves by a factor of two. A similar behavior of having the ZFC curve higher than the FC curve has previously been observed in nanocrystalline nickel ferrite [34]. As shown in Fig. 6, an applied field of 1000 Oe is sufficient to overcome the blocking effects, resulting in the ZFC-FC curves overlapping.

## 4 Conclusion

The hydrothermal approach was used to successfully synthesize  $\text{ZnFe}_2\text{O}_4$  ferrite nanoparticles with sizes of nearly 15 nm. The produced ferrite nanoparticles were cubic and single phase, according to XRD measurements. The structural analysis showed that the average crystallite size, the density, and the lattice constant of the ferrite nanoparticles were 15 nm, 5.35 g/cm<sup>3</sup>, and 8.4263 Å, respectively. The nanoparticles were monodisperse and spherical in shape, as shown by TEM measurements. The formation of a single-phase spinel

structure with two sub-lattices, tetrahedral and octahedral, was confirmed by FT-IR results. According to the magnetic measurements, the ferrite nanoparticles were found to be ferrimagnetic dressed with spin-glass behavior below  $T_B$  and superparamagnetic above  $T_B$ . The measured values of  $M_s$  and  $K_1$  were found to increase with reducing temperature. The estimated superparamagnetic critical size,  $D_{SP}$ , of the nanoparticles was found to be about 13 nm, suggesting that the prepared ferrite nanoparticles were within the superparamagnetic regime and thus by implication within the single domain regime. I believe that understanding of origins and mechanisms of superparamagnetism and spin-glass behavior in these ferrite nanoparticles is expected to have a broad impact on utilizing them in several applications, mainly in gas sensors and biomedical applications.

**Acknowledgements** The author gratefully acknowledges the financial support provided by the Deanship of Scientific Research at Hashemite University under project number 75/2017.

## Declarations

**Conflict of Interest** The author declares that he has no conflict of interests.

## References

- Mounkachi, O., Lamouri, R., Abraime, B., Ez-Zahraouy, H., El Kenz, A., Hamedoun, M., Benyoussef, A.: Exploring the magnetic and structural properties of Nd-doped Cobalt nano-ferrite for permanent magnet applications. *Ceram. Int.* **43**(16), 14401–14404 (2017)
- Al-Hadeethi, Y., Al-Heniti, S., Umar, A.: Highly sensitive hydroquinone chemical sensor based on Cd<sub>0</sub>.5Mg<sub>0</sub>.4Ca<sub>0</sub>.1Fe<sub>2</sub>O<sub>4</sub> nanoparticles. *Sci. Adv. Mater.* **9**(12), 2196–2201 (2017)
- Frey, N.A., Peng, S., Cheng, K., Sun, S.: Magnetic nanoparticles: synthesis, functionalization, and applications in bioimaging and magnetic energy storage. *Chem. Soc. Rev.* **38**(9), 2532–2542 (2009)
- Kamran, M., Anis-ur-Rehman, M.: Enhanced transport properties in Ce doped cobalt ferrites nanoparticles for resistive RAM applications. *J. Alloys and Compd.* **822**, 153583 (2020)
- Kefeni, K.K., Msagati, T.A., Mamba, B.B.: Ferrite nanoparticles: synthesis, characterisation and applications in electronic device. *Mater. Sci. Eng. B* **215**, 37–55 (2017)
- Reddy, L.H., Arias, J.L., Nicolas, J., Couvreur, P.: Magnetic nanoparticles: design and characterization, toxicity and biocompatibility, pharmaceutical and biomedical applications. *Chem. Rev.* **112**(11), 5818–5878 (2012)
- Hedayatnasab, Z., Abnisa, F., Daud, W.M.A.W.: Review on magnetic nanoparticles for magnetic nanofluid hyperthermia application. *Mater. Des.* **123**, 174–196 (2017)
- Wu, K., Li, J., Zhang, C.: Zinc ferrite based gas sensors: A review. *Ceram. Int.* **45**(9), 11143–11157 (2019)
- Lv, H., Ma, L., Zeng, P., Ke, D., Peng, T.: Synthesis of floriated ZnFe<sub>2</sub>O<sub>4</sub> with porous nanorod structures and its photocatalytic hydrogen production under visible light. *J. Mater. Chem.* **20**(18), 3665–3672 (2010)
- Goldman, A.: *Modern Ferrite Technology*. Springer Science & Business Media US (2006)
- Hasirci, C., Karaagac, O., Köçkar, H.: Superparamagnetic zinc ferrite: A correlation between high magnetizations and nanoparticle sizes as a function of reaction time via hydrothermal process. *J. Magn. Magn. Mater.* **474**, 282–286 (2019)
- Singhal, S., Namgyal, T., Bansal, S., Chandra, K.: Effect of Zn substitution on the magnetic properties of cobalt ferrite nanoparticles prepared via sol-gel route. *J. Electromagn. Anal. Appl.* **2**(6), 376–381 (2010)
- Vinnik, D., Zhivulin, V., Sherstyuk, D., Starikov, A.Y., Zezulina, P., Gudkova, S., Zherebtsov, D., Rozanov, K., Trukhanov, S., Astapovich, K., *et al*: Electromagnetic properties of zinc–nickel ferrites in the frequency range of 0.05–10 GHz. *Materials Today Chemistry.* **20**, 100460 (2021)
- Bid, S., Pradhan, S.: Preparation of zinc ferrite by high-energy ball-milling and microstructure characterization by Rietvelds analysis. *Mater. Chem. Phys.* **82**(1), 27–37 (2003)
- Mathew, D.S., Juang, R.-S.: An overview of the structure and magnetism of spinel ferrite nanoparticles and their synthesis in microemulsions. *Chemical. Eng. J.* **129**(1–3), 51–65 (2007)
- Alzoubi, G.M.: Probing the structural and magnetic properties of small crystalline nickel ferrite nanoparticles near the upper size limit of the single-domain regime. *Adv. Appl. Ceram.* **119**(4), 224–232 (2020)
- Alzoubi, G.M., Albiss, B., Shatnawi, M., Bsoul, I., Alsmadi, A., Salameh, B., Alnawashi, G.: Influence of High-Temperature Annealing on Structural and Magnetic Properties of Crystalline Cobalt Ferrite Nanoparticles in the Single-Domain Regime. *J. Supercond. Nov. Magn.* **33**(10), 3179–3188 (2020)
- Young, R.A.: *The Rietveld Method vol. 5. International union of crystallography* (1993)
- Sickafus, K.E., Hughes, R.: *Spinel compounds: structure and property relations* (1999)
- Gomes, J., Sousa, M., Tourinho, F., Mestnik-Filho, J., Itri, R., Depeyrot, J.: Rietveld structure refinement of the cation distribution in ferrite fine particles studied by X-ray powder diffraction. *J. Magn. Magn. Mater.* **289**, 184–187 (2005)
- Nikam, D.S., Jadhav, S.V., Khot, V.M., Bohara, R., Hong, C.K., Mali, S.S., Pawar, S.: Cation distribution, structural, morphological and magnetic properties of Co<sub>1-x</sub>Zn<sub>x</sub>Fe<sub>2</sub>O<sub>4</sub> (x=0–1) nanoparticles. *RSC Adv.* **5**(3), 2338–2345 (2015)
- Xu, S.-T., Ma, Y.-Q., Xu, Y.-F., Sun, X., Geng, B.-Q., Zheng, G.-H., Dai, Z.-X.: Pure dipolar-interacted CoFe<sub>2</sub>O<sub>4</sub> nanoparticles and their magnetic properties. *Mater. Res. Bull.* **62**, 142–147 (2015)
- Dippong, T., Levei, E.A., Deac, I.G., Neag, E., Cadar, O.: Influence of Cu<sup>2+</sup>, Ni<sup>2+</sup>, and Zn<sup>2+</sup> Ions Doping on the Structure, Morphology, and Magnetic Properties of Co-Ferrite Embedded in SiO<sub>2</sub> Matrix Obtained by an Innovative Sol-Gel Route. *Nanomaterials.* **10**(3), 580 (2020)
- Samoila, P., Cojocaru, C., Cretescu, I., Stan, C.D., Nica, V., Sacarescu, L., Harabagiu, V.: Nanosized spinel ferrites synthesized by sol-gel autocombustion for optimized removal of azo dye from aqueous solution. *J. Nanomaterials.* **2015** (2015)
- Choi, E.J., Ahn, Y., Hahn, E.J.: Size dependence of the magnetic properties in superparamagnetic zinc-ferrite nanoparticles. *J. Korean Phys. Soc.* **53**(4), 2090–2094 (2008)
- Coey, J.M.: *Magnetism and Magnetic Materials*. Cambridge university press (2010)
- Zhang, H., Zeng, D., Liu, Z.: The law of approach to saturation in ferromagnets originating from the magnetocrystalline anisotropy. *J. Magn. Magn. Mater.* **322**(16), 2375–2380 (2010)
- Iacovita, C., Florea, A., Scoros, L., Pall, E., Dudric, R., Moldovan, A.I., Stiufuc, R., Tetean, R., Lucaci, C.M.: Hyperthermia, Cytotoxicity, and Cellular Uptake Properties of Manganese and Zinc Ferrite Magnetic Nanoparticles Synthesized by a Polyol-Mediated Process. *Nanomaterials.* **9**(10), 1489 (2019)

29. Praveena, K., Sadhana, K.: Ferromagnetic properties of Zn substituted spinel ferrites for high frequency applications. *Int. J. Sci. Res. Publ.* **5**(4), 1–21 (2015)
  30. Mohamed, W., Alzaid, M., SM Abdelbaky, M., Amghouz, Z., García-Granda, S., M Abu-Dief, A.: Impact of Co<sup>2+</sup> Substitution on Microstructure and Magnetic Properties of Co<sub>x</sub>Zn<sub>1-x</sub>Fe<sub>2</sub>O<sub>4</sub> Nanoparticles. *Nanomaterials.* **9**(11), 1602 (2019)
  31. Nairan, A., Khan, M., Khan, U., Iqbal, M., Riaz, S., Naseem, S.: Temperature-dependent magnetic response of antiferromagnetic doping in cobalt ferrite nanostructures. *Nanomaterials.* **6**(4), 73 (2016)
  32. Li, Q., Kartikowati, C.W., Horie, S., Ogi, T., Iwaki, T., Okuyama, K.: Correlation between particle size/domain structure and magnetic properties of highly crystalline Fe<sub>3</sub>O<sub>4</sub> nanoparticles. *Sci. Rep.* **7**(1), 1–7 (2017)
  33. Kollu, P., Prathapani, S., Varaprasadarao, E.K., Santosh, C., Mallick, S., Grace, A.N., Bahadur, D.: Anomalous magnetic behavior in nanocomposite materials of reduced graphene oxide-Ni/NiFe<sub>2</sub>O<sub>4</sub>. *Appl. Phys. Lett.* **105**(5), 052412 (2014)
  34. Chinnasamy, C., Narayanasamy, A., Ponpandian, N., Chattopadhyay, K., Shinoda, K., Jeyadevan, B., Tohji, K., Nakatsuka, K., Furubayashi, T., Nakatani, I.: Mixed spinel structure in nanocrystalline NiFe<sub>2</sub>O<sub>4</sub>. *Phys. Rev. B.* **63**(18), 184108 (2001)
- Publisher's Note** Springer Nature remains neutral with regard to jurisdictional claims in published maps and institutional affiliations.